*Research Article*

# Seismic Response Analysis of Secondary Lining Polymer Grouting Debonding Repair for Tunnel Construction Based on Parameter Inversion

**Fengyang Miao [ID],[1] Chunyu Liang [ID],[2] Weiguo Li [ID],[3] Zhengxuan Huang [ID],[4] Jianguo Xu [ID],[1] Yingchun Cai [ID],[1] Xiaoyu Feng [ID],[3] and Yiming Xu [ID][5]**

[1]*College of Water Conservancy Science and Engineering, Zhengzhou University, Zhengzhou 450000, China*
[2]*Yellow River Engineering Consulting Co Ltd, Zhengzhou 450003, China*
[3]*Henan Highway Engineering Bureau Group Co Ltd, Zhengzhou 450052, China*
[4]*Hefei Gotion High-Tech Power Energy Co Ltd, Hefei 230000, China*
[5]*Sippr Engineering Group Co Ltd, Zhengzhou 450003, China*

Correspondence should be addressed to Jianguo Xu; jianguoxu@zzu.edu.cn

The void phenomenon behind the tunnel lining has become the main cause of tunnel disease, easily triggering tunnel lining structure damage, shedding, water seepage, and other diseases that seriously threaten the normal operation of the tunnel. The void area behind the lining seriously reduces the seismic capacity of the tunnel. In this paper, the mechanical parameters of the surrounding rock are calculated by optimizing the inversion of the improved system identification sensitivity analysis method, and the numerical model of the tunnel's dynamic response is optimized using the improved inversion results to study the repair effect and seismic capacity of the Longmenshan tunnel using polymer grouting to repair the void area behind the lining under the action of a seismic load. The results show that the displacement and stress at the top of the tunnel secondary lining void area are significantly reduced and close to normal after the repair of polymer grouting; however, the stress and displacement at the top of the secondary lining are significantly different under the action of seismic waves at the same peak at different site conditions, which indicates that the dynamic response of this tunnel model has obvious sensitivity to the seismic wave spectrum.

## 1. Introduction

Over the past few decades, there have been many reports of varying degrees of tunnel damage caused by earthquakes, such as the Tokachi-Oki (Japan) earthquake in 1952, the Tonghai (China) earthquake in 1970, the Chi-Chi (Taiwan, China) earthquake in 1999, the Niigataken-Chetu (Japan) earthquake in 2004, the Wenchuan (China) earthquake in 2008, and the Kumamoto (Japan) earthquake in 2016 [1]. Scholars such as Ye et al. [2–5] found that voids behind the lining are common in tunnels and have become the main cause of tunnel disease. Xin et al. studied the seismic response and damage patterns of tunnels with/without voids behind the linings by shaking table tests [6]. Yasuda et al. studied the seismic response of cylindrical tunnels with void areas under 3D earthquakes, and the results showed that the large stress concentration on the lining caused by voids under the action of the earthquake resulted in the destruction of the tunnel [7]. Min et al. studied the effect of voids behind linings on the cracking performance of asymmetric double-arch tunnels, and the results show that due to the influence of the void area, the cracking of the tunnel area opposite the void area is more serious [8]. The research of the above scholars shows that the void area behind the tunnel lining seriously reduces the seismic performance of the tunnel, the lining in the void area

generates tensile stresses under seismic action, and the surrounding rock around the void area deforms severely in plasticity, leading to rockfall impacting the lining and serious lining damage.

The demolition and reconstruction method, backfill grouting method, and shotcrete concrete combined with the steel arch reinforcement method are often used to repair and fill void areas [9]. Jinlong et al. used secondary grouting to repair the void area of the tunnel. During the secondary grouting process, it was found that higher grouting pressure, a larger grout amount, and improper grouting position would lead to cracks in the tunnel [10]. In order to solve the problem of tunnel disease caused by cracks in the tunnel lining, Zhou et al. adopted the plate-short bolt assembly structure to reinforce the tunnel cracks [11]. Han et al. explored the reinforcement effect of the fiber-reinforced plastic (FRP)-polymer cement mortar (PCM) method on the void area of the tunnel [12]. Liu et al. used crack grouting, shotcrete support, and reconstruction of the secondary lining to repair the damaged lining [13]. However, due to the inherent defects of concrete, which limit the effect of tunnel disease management, many scholars have applied polymer grouting technology to tunneling projects in view of the advantages of early strength, lightweight, and good durability of polymer materials [14, 15]. At present, the research in this field mainly focuses on the rapid repair of buried pipeline leakage and settlement, railway track settlement, and pavement voids and collapse. Wang et al. repaired the void under the pipeline with polymer, and the results showed that polymer grouting can effectively restore the strength and resilience of the pipeline to its normal state [16, 17]. Li et al. developed an innovative trenchless concrete pipeline corrosion and void defect pretreatment technology called membrane bag pile polymer grouting pretreatment (MBP-PGP) technology, which can be used for pipeline corrosion and voiding repair [18]. Fang et al. showed through experiments that polymers can effectively repair the settlement of high-speed railways and provide sufficient long-term durability under dynamic train loads [19, 20]. The research of Li et al. shows that high polymer can effectively repair cracks and voids in pavement and effectively prevent pavement settlement [21, 22]. The polymer grouting material can sufficiently and densely fill the damaged area, thereby controlling the unfavorable deformation and better restoring the structural integrity. Therefore, the combination of polymer grouting repair technology and tunnel nondestructive testing can quickly find and repair tunnel disaster problems.

The abovementioned study did not investigate the effect of the seismic response of the tunnel after polymer grouting repair. This paper takes the Longmenshan tunnel project as an example. In order to simulate the Longmenshan tunnel more precisely, this paper deduces the inversion formula of the three-dimensional parameters of the physical mechanics of the surrounding rock of the tunnel based on the basic theory of system identification and improves the inversion method with the help of numerical simulation software. The improved inversion results are used to optimize the mechanical parameters of the surrounding rock of the tunnel and then study the repair effect and seismic capacity of the Longmenshan tunnel using polymer grouting to repair the void area behind the lining under the action of an earthquake load so as to provide the tunnel void space. Polymer grouting repair provides a theoretical basis.

## 2. Project Overview

Longmenshan Mountain tunnel is located at the junction of Tangchi town of Liuan city and Daguan town of Tongcheng city, Anhui province, China. It is a detached tunnel, buried at a depth of 50 m–300 m, with starting pile number K81 + 834 (ZK81 + 830) and ending pile number K84 + 47 (ZK84 + 450), a total length of 2644 (2620 m). The surrounding rock grade of the tunnel is mainly III, IV, and V grades surrounding rock, where III and IV grades surrounding rock is mainly medium weathered granite, and V grade surrounding rock is mainly full weathered granite.

*2.1. Tunnel Construction Monitoring and Measurement.* As is shown in Figure 1, the measurement items of the Longmenshan tunnel include surface subsidence observation, vault subsidence observation, and peripheral convergence measurement. As shown in the arch settlement diagram (Figure 2) of the K83 + 020 void section of the Longmenshan tunnel, the surrounding rock basically reached a stable state after 40 days, the accumulated settlement value was kept below 10 mm, and the development trend of the arch settlement curve was approximately a logarithmic function curve, which was finally kept at 9.4 mm. As is shown in Figure 3. The settlement rate of the vault also tended to decrease slowly on the whole, and after 40 days, the settlement rate remained relatively stable, between 0.1 mm/d and 0 mm/d. The maximum settlement rate was 0.6 mm/d on day 5, which occurred during the excavation of the lower step. Due to the relatively short duration of the maximum change in the settlement rate, it would not have much impact on the overall stability and safety of the tunnel excavation process. Overall, the vault deformation of this section is in a reasonable range at all stages; no abnormality is seen, the surrounding rock is basically stable, and the excavation method is reasonable.

As is shown in Figure 4, analysis of the convergence deformation data around the K83 + 020 void section of the Longmenshan tunnel right line shows that the accumulated peripheral convergence value of this section is smaller than the arch settlement value, and the regularity of its deformation process is more scattered than that of the arch deformation, and the result still tends to convergence. As is shown in Figure 5, analysis of the convergence deformation data around the K83 + 020 void section of the Longmenshan tunnel right line shows that during the whole process of convergence deformation, the convergence rate is higher in the first period, the peak reaches 0.4 mm/d, the duration is still short, and then drops sharply, the convergence rate is stabilized between 0.3 mm/d and 0.1 mm/d, the phenomenon of negative growth of convergence deformation appears in the 25th day, and there is no obvious sign of damage to the
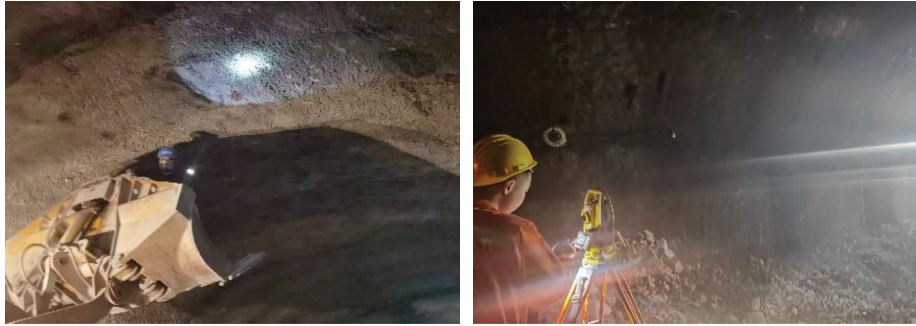
Figure 1: LongmenShan tunnel right line K83 + 020 void cross-section monitoring and measurement data.
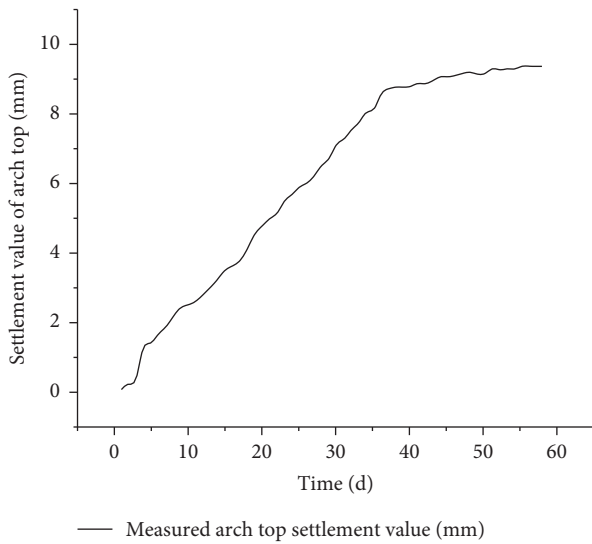


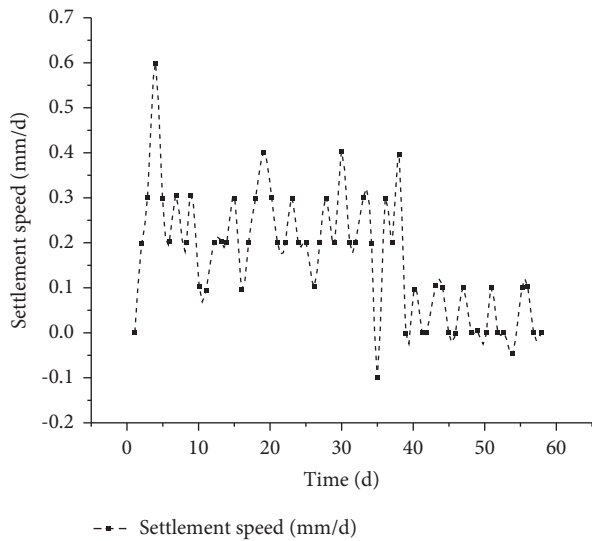Figure 2: Settlement curve of K83 + 020 void section vault.



Figure 3: Settlement rate curve of K83 + 020 void section vault.

cave body in this process. After the 40th day, the convergence value of the cave body was kept at about 7 mm, and it could be affirmed as basic convergence when it reached 7.3 mm. The convergence rate was stabilized within 0.1 mm/ d at the end, and the cave was basically stable without any abnormalities.

## 3. Numerical Simulation of Tunnel Excavation

*3.1. Tunnel Excavation Process Simulation.* Numerical simulation object for Longmenshan tunnel right line K83 + 010~K83 + 90 section, excavation length 80 m, tunnel burial depth of about 100~110 m, the terrain is relatively gentle, the section is IV grade surrounding rock, rock type for the medium weathering granite, the tunnel using the up-and-down step method of boring. The tunnel is excavated by the up-and-down step method. The inner contour of the main tunnel of the tunnel is a three-centered circle with diameters of 10.5 m, 12.8 m, and 10.5 m, respectively. The total height of the main tunnel is 7.45 m, and the total width is 11.93 m. For the creation of soil, according to Saint-Venant's principle, the stress redistribution caused by excavation is only within the range of 3–5 times the excavation width from the cavern, and will not cause too much impact on other areas. Therefore, the left and right boundaries of the model are three times the diameter of the tunnel, and the width is 100 m. The lower boundary is 3.5 times the diameter of the hole. According to the real terrain, the height is selected to be 150–160 m. The height of the tunnel from the bottom of the soil is 50 m, and the buried depth is 100–110 m. Combined with the tunnel ground investigation report, the soil model adopts the Mohr–Coulomb model in the elastoplastic principal model. The physical parameters of the soil are its density of 1.8 g/cm$^3$, modulus of elasticity of 2.6 GPa, Poisson's ratio of 0.32, friction angle of 34°, and cohesion of 0.5 MPa. The overrun support structure of the tunnel is a Φ25 mm overrun hollow grouting anchor with a density of 7.8 g/cm$^3$, a modulus of elasticity of 200 GPa, and Poisson's ratio of 0.2. The lining is made of C25 plain waterproof concrete; the density is 2.4 g/cm$^3$, the elastic modulus is 20 GPa, and Poisson's ratio is 0.2. The inverted arch and the secondary lining are made of C30 concrete with a density of 2.5 g/cm$^3$ and an elastic modulus of 25 GPa and Poisson's ratio of 0.2. The lining and the surrounding rock are bound together by tie constraints. Normal constraints were applied to the front, back, left, and right boundaries of the tunnel model, with the bottom boundary being fully constrained and the upper boundary being free. The vertical
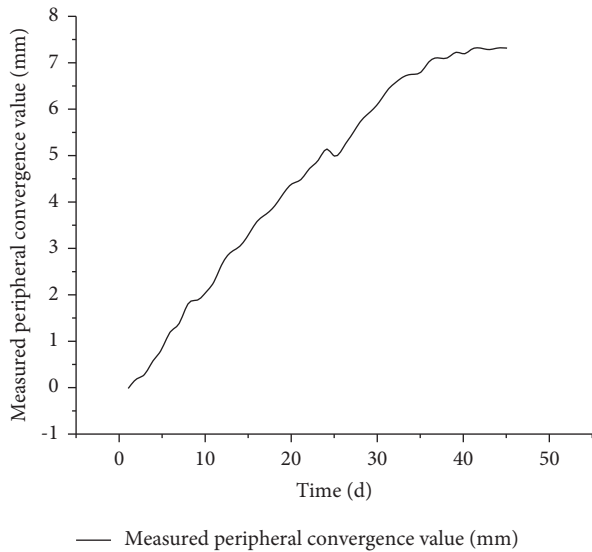
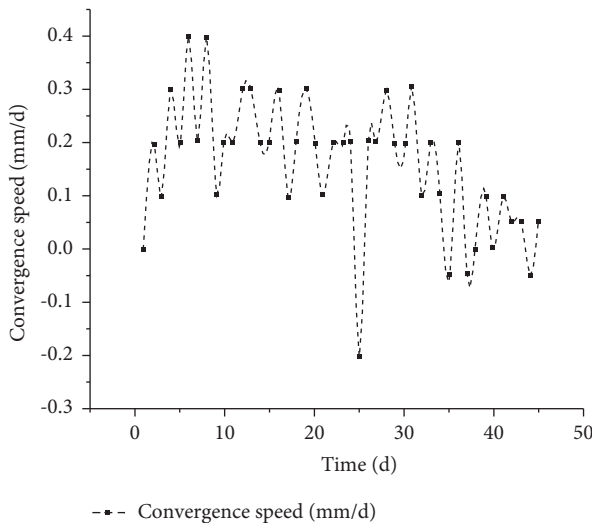Figure 4: Peripheral convergence curve of K83 + 020 void section.



Figure 5: Peripheral convergence rate curve of K83 + 020 void section.

better verify the accuracy of the numerical model, the vertical displacement at monitoring point 1 of the liner and the summation of the transverse displacement at monitoring points 2 and 3 were extracted (the locations of the points taken are shown in Figure 8), plotted as curves, and analyzed to compare the deformation trend of the measured vault subsidence value and the peripheral convergence value of the section where the liner is located.

As shown in Figure 9, a comparison of the analysis of the settlement values of the vault (the vertical displacement value at monitoring point 1) of void section K83 + 020, the peripheral convergence values (the sum of the lateral displacement values at monitoring points 2 and 3), and the calculated values of the model simulation reveals that the analysis results obtained also differ from the real situation due to the difference between the selected soil mechanical parameters and the real surrounding rock mechanical parameters. However, the theoretical analysis of the change in the initial lining displacement during the numerical simulation of tunnel excavation is consistent with the deformation law of the real tunnel excavation process, indicating that the numerical simulation of the Longmenshan Mountain tunnel excavation process is consistent with the real excavation process and the difference in stress and strain is caused by the unreasonable setting of the mechanical parameters of the tunnel surrounding rock during the simulation process, which can be analyzed by the inversion of the surrounding rock mechanical parameters to obtain The inversion analysis of the mechanical parameters of the surrounding rock can be used to obtain the mechanical parameters of the surrounding rock that are close to the real situation.

## 4. Inversion Analysis of Tunnel Envelope Mechanical Parameters

*4.1. 3D Mechanical Parameter Inversion Analysis of Surrounding Rock.* Some scholars [23–29] have already applied the system identification sensitivity analysis method in the inverse calculation of layered pavement structure, foundation excavation deformation analysis, and asphalt pavement aging inversion analysis, but at present, the system identification sensitivity analysis method is mainly applied to the inversion of two-dimensional parameters of tunnel envelope, and less tunnel monitoring data are used in the inversion analysis. In this paper, based on the forward model established for the Longmenshen Mountain tunnel as the Mohr–Coulomb 3D numerical model, a system identification method is introduced in the field of 3D parameter inversion analysis of the tunnel envelope. As shown in Figure 10, the three parameters of static elastic modulus, Poisson's ratio, and internal friction angle of the surrounding rock are calculated by inversion based on the measured peripheral convergence value $S_1'$, vault settlement value $S_2'$, and vault settlement value $S_3'$ of the measured section of a tunnel, which can realize the high-precision and efficient automation of the model parameter adjustment process, and the basic process is as follows:

downward gravity load acts on the whole model. The overall meshing of the tunnel model is sparse in the overall soil and dense in the boundary of the tunnel. The neutral axis algorithm is used. The element type of the anchor is the truss and the total number of mesh elements is 126,600. The tunnel model of the lattice is shown in Figure 6.

*3.2. Analysis of Results.* It can be seen from Figure 7 that the top of the arch is the maximum vertical displacement of the primary support structure, which reaches 6.267 mm. The maximum lateral displacement of 2.456 mm occurred in the arch waist area, while the measured settlement value of the arch top and the convergence value around the target section were 9.4 mm and 7.3 mm, respectively, with a large difference of 3.133 mm in the accumulated vault settlement value and 2.31 mm in the accumulated convergence value. To
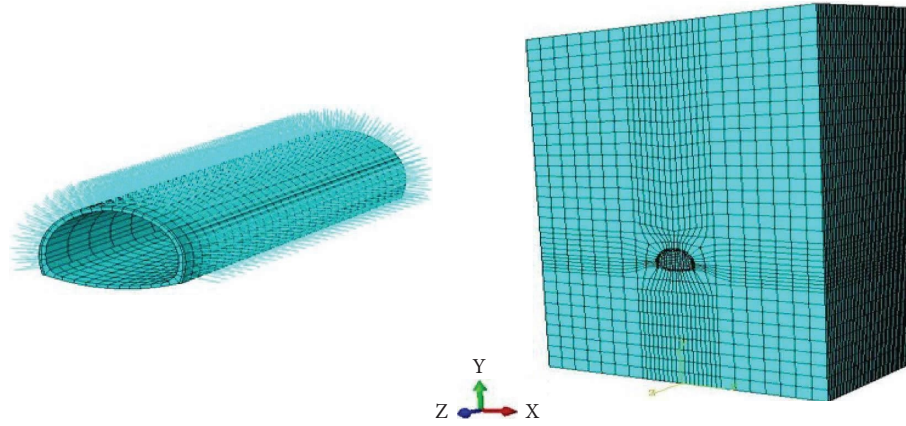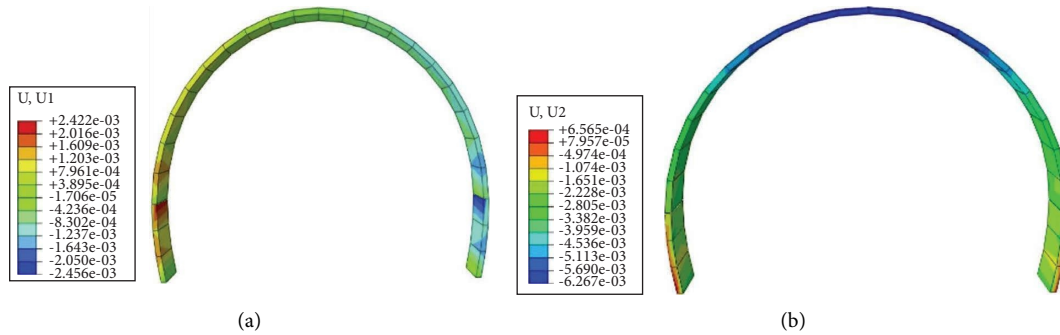
FIGURE 6: Tunnel model.



FIGURE 7: LongMianShan tunnel right line K83 + 020 section initial lining, transverse displacement cloud map, and vertical displacement cloud map: (a) a transverse displacement cloud map of the initial lining when the surrounding rock is stable; (b) a vertical displacement cloud map of the initial lining when the surrounding rock is stable.
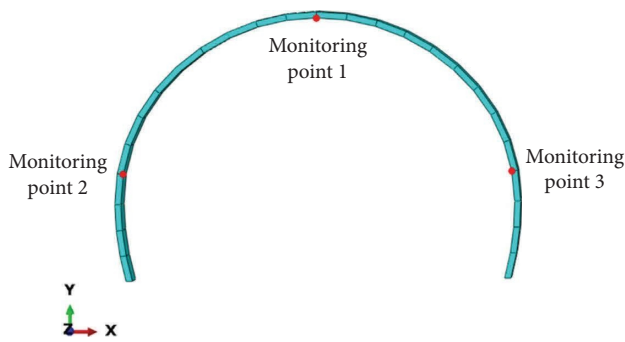


FIGURE 8: Location of the target section's primary lining monitoring points in the tunnel model.

(1) Setting the initial surrounding rock mechanical parameters

The initial internal friction angle $\varphi_0$, the modulus of elasticity $E_0$, and the initial Poisson's ratio $\mu_0$ are assumed. $\varphi_0$, $E_0$, and $\mu_0$ are input into the finite element forward model to calculate the displacement values of the section corresponding to the measured values

$$\{s\} = \begin{bmatrix} s_1 & s_2 & s_3 \end{bmatrix}^T. \tag{1}$$

(2) Comparing the calculated value $\{s\}$ with the measured value $\{s'\}$

If the absolute value of the difference between the calculated value and the measured value is small, that is, the calculated result meets the requirements, take $\max\left\{\{\Delta s\}^T \{\Delta s\}\right\} \leq e$ ($e$ is the calculation accuracy), immediately terminate the inverse analysis calculation, at this time the model elastic modulus $E$, Poisson's ratio $\mu$ and internal friction angle $\varphi$ is the actual surrounding rock material static elastic modulus $E_s$, Poisson's ratio $\mu$ and internal friction angle $\varphi$.

(3) Establishing the sensitivity matrix

Using the forward difference method to build the sensitivity matrix, we find the calculated values $\{s(E_0, \mu_0, \varphi_0)\}$ for the initial elastic modulus $E_0$, initial Poisson's ratio $\mu_0$, and initial internal friction angle $\varphi_0$; then we find $\{s(E_0 + \Delta E, \mu_0, \varphi_0)\}$ for the elastic modulus $E_0 + \Delta E$, Poisson's ratio $\mu_0$, and internal friction angle $\varphi_0$; then we find $\{s(E_0, \mu_0 + \Delta\mu, \varphi_0)\}$; for the elastic modulus is $E_0$, the internal friction angle $\varphi_0$, and Poisson's ratio is $\mu_0 + \Delta\mu$; then find the $\{s(E_0, \mu_0, \varphi_0 + \Delta\varphi)\}$ when the modulus of elasticity $E_0$ Poisson's ratio $\mu_0$ is constant, and the internal friction angle is $\varphi_0 + \Delta\varphi$ by taking $\Delta E = 1\% E$, $\Delta E = \Delta\mu = 1\%\mu$, and $\Delta\varphi = 1\%\varphi$ thus getting
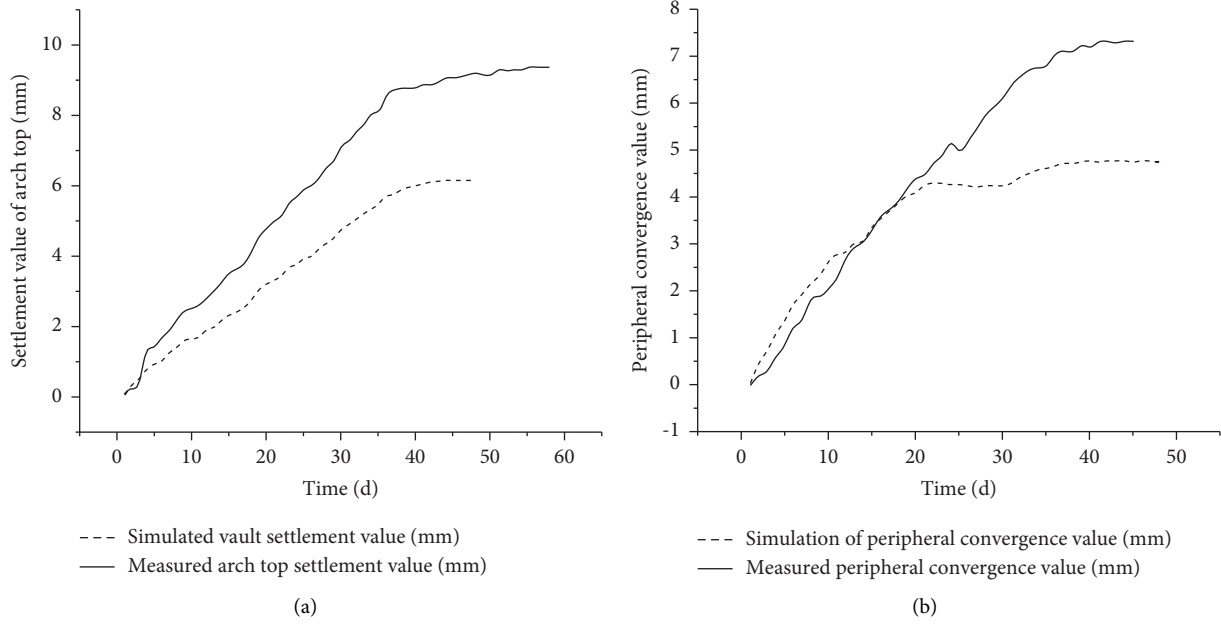
FIGURE 9: Comparison of measured and simulated values of vault settlement and peripheral convergence at void section K83 + 020: (a) comparison between measured and simulated values of vault settlement (monitoring point 1); (b) comparison between measured and simulated values of peripheral convergence (monitoring points 2 and 3).

$$
\begin{cases}
\dfrac{\partial s_1}{\partial E} = \dfrac{s_1\left(E_0 + \Delta E, \mu_0, \varphi_0\right) - s_1\left(E_0, \mu_0, \varphi_0\right)}{\Delta E}, \\[2mm]
\dfrac{\partial s_1}{\partial \mu} = \dfrac{s_1\left(E_0, \mu_0 + \Delta \mu, \varphi_0\right) - s_1\left(E_0, \mu_0, \varphi_0\right)}{\Delta \mu}, \\[2mm]
\dfrac{\partial s_1}{\partial \omega} = \dfrac{s_1\left(E_0, \mu_0, \varphi_0 + \Delta \varphi\right) - s_1\left(E_0, \mu_0, \varphi_0\right)}{\Delta \varphi}, \\[2mm]
\dfrac{\partial s_2}{\partial E} = \dfrac{s_2\left(E_0 + \Delta E, \mu_0, \varphi_0\right) - s_2\left(E_0, \mu_0, \varphi_0\right)}{\Delta E}, \\[2mm]
\dfrac{\partial s_2}{\partial \mu} = \dfrac{s_2\left(E_0, \mu_0 + \Delta \mu, \varphi_0\right) - s_2\left(E_0, \mu_0, \varphi_0\right)}{\Delta \mu}, \\[2mm]
\dfrac{\partial s_2}{\partial \omega} = \dfrac{s_2\left(E_0, \mu_0, \varphi_0 + \Delta \varphi\right) - s_2\left(E_0, \mu_0, \varphi_0\right)}{\Delta \varphi}, \\[2mm]
\dfrac{\partial s_3}{\partial E} = \dfrac{s_3\left(E_0 + \Delta E, \mu_0, \varphi_0\right) - s_3\left(E_0, \mu_0, \varphi_0\right)}{\Delta E}, \\[2mm]
\dfrac{\partial s_3}{\partial \mu} = \dfrac{s_3\left(E_0, \mu_0 + \Delta \mu, \varphi_0\right) - s_3\left(E_0, \mu_0, \varphi_0\right)}{\Delta \mu}, \\[2mm]
\dfrac{\partial s_3}{\partial \omega} = \dfrac{s_3\left(E_0, \mu_0, \varphi_0 + \Delta \varphi\right) - s_3\left(E_0, \mu_0, \varphi_0\right)}{\Delta \varphi}.
\end{cases}
\tag{2}
$$

(4) Calculating the parameter adjustment vector $\{\Delta x\}$

Calculating the difference $\{\Delta s\} = \{s\} - \{s'\} = \begin{Bmatrix} s_1 - S_1' \\ s_2 - S_2' \\ s_3 - S_3' \end{Bmatrix}$ between the measured values and the calculated values under the initial modulus of elasticity $E_0$, the initial Poisson's ratio $\mu_0$, and the initial angle of internal friction $\varphi_0$. Then, construct the sensitivity equation

$$
\{\Delta s\} = D\{\Delta x\}, \tag{3}
$$

where the sensitivity matrix $D = \begin{bmatrix} \partial s_1/\partial E & \partial s_1/\partial \mu & \partial s_1/\partial \varphi \\ \partial s_2/\partial E & \partial s_2/\partial \mu & \partial s_2/\partial \varphi \\ \partial s_3/\partial E & \partial s_3/\partial \mu & \partial s_3/\partial \varphi \end{bmatrix}$ and the parameter adjustment vector $\{\Delta x\} = \begin{bmatrix} \Delta E \\ \Delta \mu \\ \Delta \varphi \end{bmatrix}$.

The difference $\{\Delta s\}$ between the measured values and the calculated values under the initial elastic modulus $E_0$, the initial Poisson's ratio $\mu_0$, the initial internal friction angle $\varphi_0$, and the sensitivity matrix $D$ is input to the prepared numerical analysis program, which will calculate the parameter adjustment vector $\{\Delta x\}$.

(5) Performing the first iteration

Establishing the following equation:

$$
\begin{cases}
E_1 = E_0 + \Delta E, \\
\mu_1 = \mu_0 + \Delta \mu, \\
\varphi_1 = \varphi_0 + \Delta \varphi.
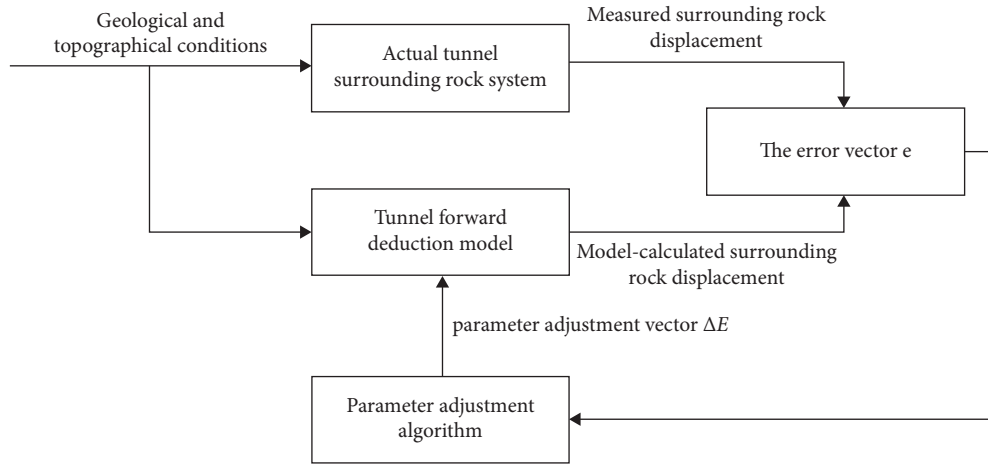\end{cases}
\tag{4}
$$

FIGURE 10: The basic process of identification of tunnel envelope parameter inverse calculation system.

Finding the calculated values $\{s\}^{(1)} = \{s(E_1, \mu_1, \varphi_1)\}^{(1)}$ under the modulus of elasticity $E_1$, Poisson's ratio $\mu_1$, and the angle of internal friction $\varphi_1$, with the upper mark "(1)" representing the first parameter adjustment, and then go back to step 2 until the requirements are met.

*4.2. Inversion of Mechanical Parameters of Longmenshan Tunnel Enclosure.* After several parameter adjustments, assuming that the initial mechanical properties of the surrounding rock parameters $E_0 = 2.0\,\mathrm{GPa}, \mu_0 = 0.32, \varphi_0 = 32°$, the inversion calculation is carried out according to the 3D mechanical parameters inversion method proposed in this paper, and four iterations are carried out to obtain $E = 1.82\,\mathrm{GPa}, \mu = 0.32, \varphi = 35°$, at which time the tunnel finite element model calculates the peripheral convergence value $s_1$ as 7.2554 mm, $s_2$ is 9.5317 mm, and $s_3$ is 8.8206 mm. According to the measured cumulative peripheral convergence value $s_1'$ is 7.3224 mm, the measured cumulative vault settlement value $s_2'$ is 9.4669 mm, and the measured cumulative vault settlement value $s_3'$ is 8.7128 mm, it can be found that the simulated value is very close to the measured value as well. According to the model results, the measured results of the tunnel can be obtained, as shown in Table 1.

At this point $\{\Delta s^T\}\{\Delta s\} = 0.0466\,\mathrm{mm}$, satisfying the condition $\max\ \max\{\{\Delta s\}^T\{\Delta s\}\} \le 1.0E - 5\mathrm{m}$, the real surrounding rock mechanical parameters of the grade IV section of the Longmenshan tunnel numerically simulated are static elastic modulus $E_s = 1.82\,\mathrm{GPa}$, Poisson's ratio $\mu = 0.32$, and internal friction angle $\varphi = 35°$. Based on the system identification sensitivity analysis method for inversion to obtain the final surrounding rock parameters to establish the forward model, extract the simulated value of displacement change of its tunnel right line K83 + 020 section and the actual measurement to draw the fitting curve as shown in Figure 11.

Comparing the simulated and measured displacement variation curves of the target sections, it can be seen that the mechanical parameters obtained by applying the system identification sensitivity analysis method to the mechanical parameters of the tunnel envelope after

displacement measurement inversion analysis and then substituting into the finite element model for the forward evolution have small error between the simulation results and the measured values. In each stage of tunnel construction, the error values of vault deformation and peripheral convergence of each target section in the numerical model and the actual monitoring and measurement results are small, within 0.3 mm. Through the inversion analysis of the Longmenshan tunnel, the actual surrounding rock parameters were reasonably determined for the section from K83 + 020 to K83 + 90, with a static elastic modulus $E_s = 1.82\,\mathrm{GPa}$, Poisson's ratio $\mu = 0.32$, and an internal friction angle $\varphi = 35°$. The results all meet the requirements of highway tunnel design specifications and prove the feasibility of the system identification sensitivity analysis method, which provides important application value for the real-time detection and evaluation of the tunnel under construction in Longmenshan Mountain and provides a basis for subsequent related scientific research.

## 5. Seismic Response Analysis of Tunnel Void Polymer Grouting Repair

*5.1. Tunnel Void Inspection and Repair.* In the right line of the Longmenshan tunnel section from K83 + 140 to K83 + 350, a geological radar method was used to inspect the quality of lining construction, and it was found that there was a void area with a maximum depth of 20 cm and a longitudinal length of about 2~3 m between the lining and the rock body at the top of the tunnel, as shown in Figures 12 and 13.

According to the data provided by radar, grouting repair of the void area, compared with concrete grouting material, has excellent antiseepage performance, compressive performance, tensile performance, and corrosion resistance. After the polymer repair material reaction, it can not only rapidly occur volume expansion (volume expansion 10~20 times), but also can automatically compact and reinforce the void area, and recompact and reinforce the structural disease area. More importantly, it is light in weight, high in construction efficiency, low in time cost, and high in economy, and the polymer material can reach 90% sufficient strength

TABLE 1: Tunnel section displacement change comparison table.

| Construction stage | Lower step application initial lining | | Palm surface advance 20 m | | Palm surface advance 40 m | | Pouring of second lining | |
| --- | --- | --- | --- | --- | --- | --- | --- | --- |
| | Real measurement (mm) | Finite element model (mm) | Real measurement (mm) | Finite element model (mm) | Real measurement (mm) | Finite element model (mm) | Real measurement (mm) | Finite element model (mm) |
| Peripheral convergence (K83 + 020) | 2.6 | 2.3 | 4.7 | 4.5 | 6.5 | 6.3 | 7.3 | 7.2 |
| Vault settlement (K83 + 020) | 2.8 | 2.5 | 5.2 | 5.5 | 7.5 | 7.6 | 9.4 | 9.5 |
| Vault settlement (K83 + 040) | 3.3 | 3 | 5.4 | 5.6 | 7.7 | 7.8 | 8.7 | 8.8 |
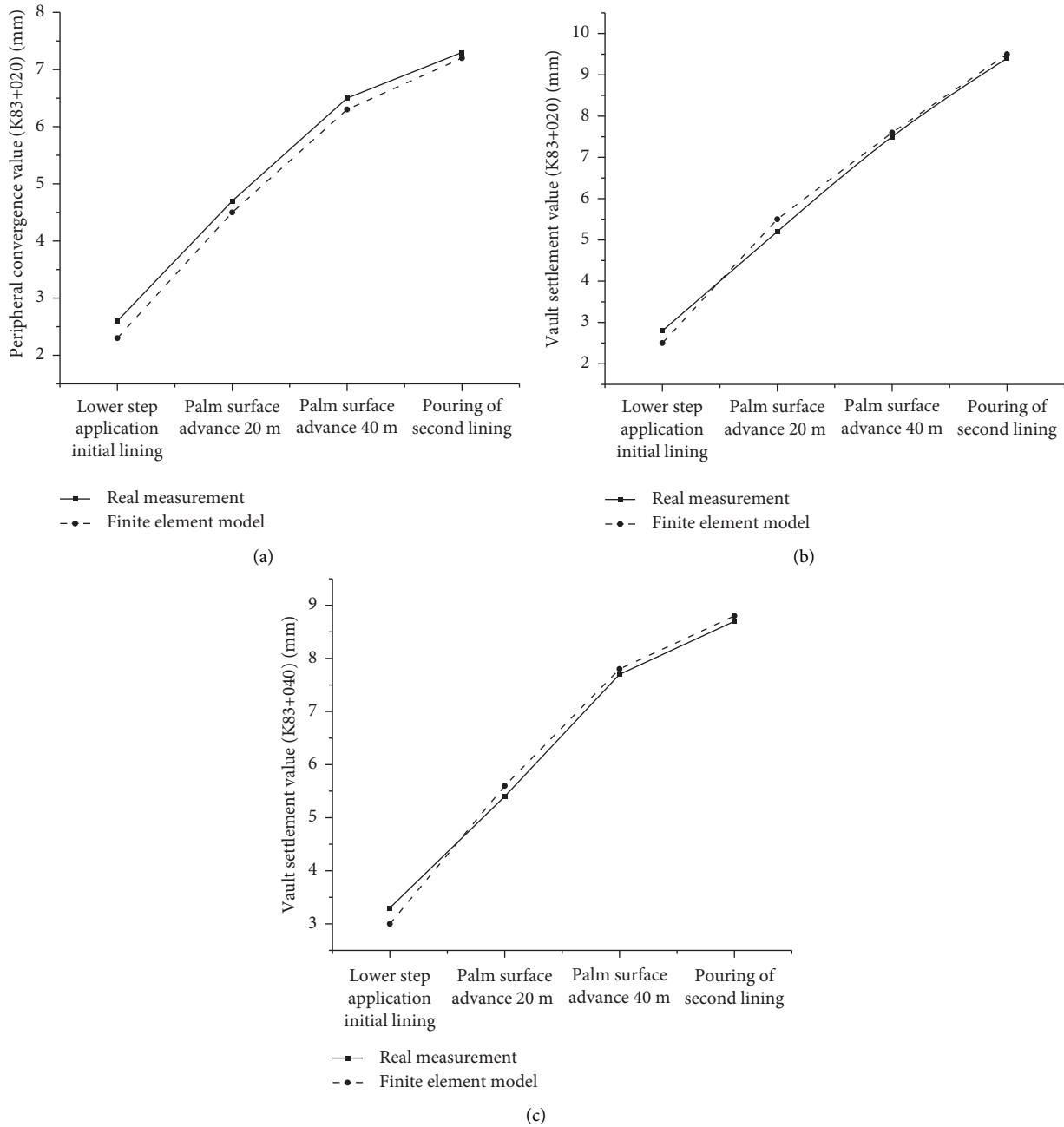
FIGURE 11: Comparison between simulated and measured values of arch top settlement in the target section of the tunnel: (a) K83 + 020 cross-sectional convergence around the simulated value and the measured value fitting curve; (b) K83 + 020 fitting curve between simulated and measured values of vault settlement; (c) K83 + 040 fitting curve between the simulated and measured values of vault settlement.

within 15 minutes after injection [16–20]. The grouting material used is a nonwater-reactive polymer. By comparing the radar detection spectra before and after the polymer grouting in Figure 14, it is found that the grouting effect in the void area behind the lining is good and that the integrity and compactness of the lining structure are significantly improved. To better verify the effect of polymer material for tunnel debonding repair, this paper carries out a comparative analysis of the seismic response before and after the tunnel polymer grouting repair under seismic action.

*5.2. Numerical Model Creation.* The numerical model was established based on the surrounding rock grade and tunnel burial depth of the Longmenshan tunnel section K83 + 140 to K83 + 350; the tunnel burial depth is 70 m the excavation depth is 160 m, and the tunnel debris area is located at the tunnel excavation depth of 80~83 m. The static modulus of elasticity $E_s = 1.82$ GPa, Poisson's ratio $\mu = 0.32$, internal friction angle $\varphi = 35°$, and the correlation between the static modulus of elasticity $E_s$ and the dynamic modulus of elasticity $E_d$ is considered according to the literature [30], which

FIGURE 12: Lining construction quality inspection site.



FIGURE 13: Void behind the lining.

results in the dynamic modulus of elasticity $E_d = 18.63$ GPa for the tunnel geotechnical body. The polymer material used for grouting is a nonwater-reactive polymer material with a density of 1.6 g/cm$^3$, an elastic modulus $E = 20.2$ MPa, and Poisson's ratio of $\mu = 0.3$. The model with a well-defined grid is shown in Figure 15. The seismic fortification standard of the Longmenshan tunnel is 0.1 g peak ground motion acceleration and 7-degree earthquake basic intensity. The three natural seismic waves selected for conducting seismic analysis are the Northridge wave (Class I site), the Taft wave (Class II site), and the EL-Centro wave (Class III site), which correspond to a peak acceleration of 0.1 g, a time interval of 0.02 s, and an effective duration of 19.2 s.

### 5.3. Analysis of the Seismic Mechanical Response of Tunnel and Grouting Repair

#### 5.3.1. Displacement Analysis of Seismic Load Action.
Since the debris area is located at the top of the tunnel, the vertical displacement and vertical acceleration at the top node of the secondary lining can visually reflect the improvement of the debris area by polymer grouting. It can be seen from Figures 16–19 that under the same earthquake, the displacement and acceleration time-history curves of the top of the secondary lining of the tunnel under normal, void, and polymer grouting repair conditions are basically the same. It can be seen that during the whole time course of vibration, the vertical displacement and vertical acceleration of the top of the secondary lining under normal conditions are the

smallest, and the vertical displacement and vertical acceleration are the largest when the top is void, which is significantly improved after grouting repair of the void area. Under each working condition of the Northridge wave action, the maximum vertical displacement at the top of the secondary lining under normal conditions, when the top is void, and after the void repair is 5.33 mm, 6.15 mm, and 5.68 mm, respectively, and the maximum vertical acceleration is 1.32 m/s$^2$, 1.56 m/s$^2$, and 1.43 m/s$^2$, respectively. Compared with the normal condition, the maximum vertical displacement at the top of the secondary lining when the top is void and after the void repair is 5.68 mm. Compared with the normal situation, the increase in maximum vertical displacement and maximum vertical acceleration at the top of the secondary lining was 15.4% and 18.5% when the top was void, and after the grouting repair, the increase of maximum vertical displacement and maximum vertical acceleration was 6.6% and 8.3%, which was 7.6% and 8.3% less than the increase when the top was void. Under the conditions of Taft wave action, the vertical displacements and vertical accelerations of the top of the secondary lining were 3.78 mm, 4.07 mm, and 3.95 mm under normal conditions, when the top was void and after the void repair, respectively, and the vertical accelerations were 1.08 m/s$^2$, 1.17 m/s$^2$, and 1.12 m/s$^2$, respectively. Compared with the normal conditions, the increase of the vertical displacement and vertical acceleration of the top of the secondary lining when the top was void was The increase of vertical displacement and vertical acceleration at the top of the secondary lining was 7.7% and 8.3% compared with the normal condition, and after the grouting repair, the increase of vertical displacement and vertical acceleration was 4.5% and 3.7%, which was 2.9% and 4.3% less than the increase at the time of top debonding. Under each working condition of the EL-Centro wave action, the vertical displacement at the top of the secondary lining under normal conditions, when the top is void and after the void repair is 2.97 mm, 3.85 mm, and 3.44 mm, respectively, and the maximum value of vertical acceleration is 0.91 m/s$^2$, 1.04 m/s$^2$, and 0.97 m/s$^2$, respectively, compared with the normal condition, the increase of vertical displacement and vertical acceleration at the top of the secondary lining when the top is void is 29.6% and 14.3%. Compared with the normal condition, the increase of vertical displacement and vertical acceleration at the top of the secondary lining was 29.6% and 14.3%, and after the grouting repair, the increase of vertical displacement and vertical acceleration was 15.8% and 6.6% compared with the normal condition, which was 10.6% and 6.7% less than the increase when the top was void. From the above analysis, it can be seen that the void has a greater impact on the tunnel, which will significantly increase the seismic response of the tunnel. After repairing the tunnel with polymer grouting, the maximum tunnel displacement will be significantly reduced, coming close to the displacement of the normal tunnel. It reflects the repair effect of polymer grouting on tunnel voids.

It can be seen from Figure 19 that, under the action of seismic waves with the same peak value in different site conditions, there are obvious differences in the vertical

(a)                                                                                          (b)
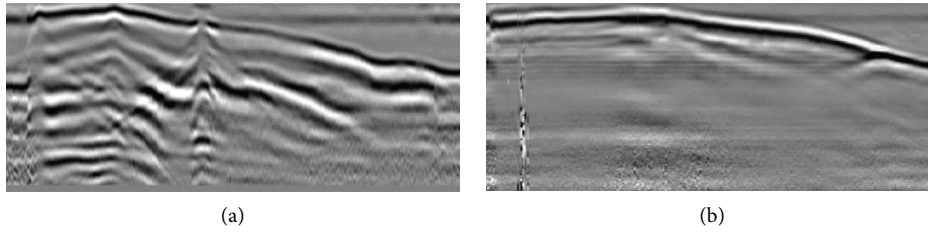
FIGURE 14: Geological radar detection spectra before and after grouting: (a) geological radar detection spectrum before polymer grouting; (b) geopolymer grouting after georadar detection spectrum.
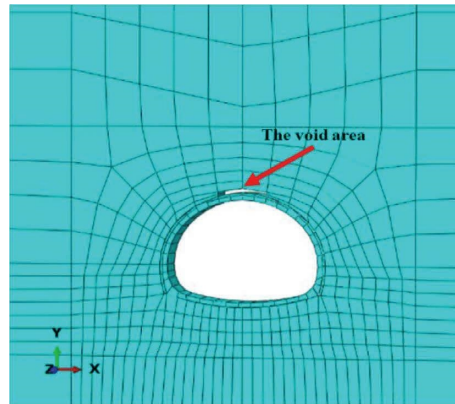


FIGURE 15: Schematic diagrams of the decommissioning area.

acceleration and vertical displacement of the top of the secondary lining. The vertical displacement and vertical acceleration of the top of the secondary lining of the tunnel under the excitation of the Northridge wave (type I site) are the largest, and the vertical displacement and vertical acceleration under the excitation of the EL-Centro wave (type III site) are the smallest. Hard, medium hard, or medium soft, the influence on the displacement and acceleration response of the top of the secondary lining gradually decreases, indicating that the dynamic response of the tunnel model has obvious seismic wave spectrum sensitivity.

*5.3.2. Stress Analysis of Seismic Load Action.* From Figures 20 to 23, it can be seen that under the three vertical seismic loads, the overall tunnel support structure in different working conditions behaves as a compressed state. Under the action of Northridge waves, the maximum absolute values of the maximum principal stresses at the top of the secondary lining in normal conditions, when the top is void, and after grouting repair are 0.211 MPa, 0.260 MPa, and 0.241 MPa, respectively, and the maximum values of the minimum absolute principal stresses are 7.49 MPa, 8.85 MPa, and 8.15 MPa. Compared with the normal condition, the increase in the maximum absolute values of the maximum principal stresses and the minimum absolute values of the principal stresses at the top of the secondary lining when the top is compared with the normal condition, the increase in the maximum absolute value of the maximum principal stress and the minimum absolute value of the principal stress at the top of the secondary lining was 23.2%

and 18.2%, and after the grouting repair, the increase in the maximum absolute value of the maximum principal stress and the minimum absolute value of the principal stress was 14.2% and 8.8% compared with the normal condition, and the increase was 7.3% and 7.9% less than the increase at the top of the lining when it was void. Under the action of Taft wave, the maximum absolute values of maximum principal stress at the top of secondary lining in normal condition, when the top is void and after grouting repair are 0.196 MPa, 0.241 MPa, and 0.218 MPa, respectively, and the maximum values of minimum absolute principal stress are 6.90 MPa, 7.95 MPa, and 7.21 MPa, compared with normal condition, the maximum values of maximum principal stress at the top when the top is void and the maximum values of minimum absolute principal stress at the top of secondary lining compared with the normal condition, the increase in the maximum value of absolute principal stress and the maximum value of absolute minimum principal stress at the top was 23.0% and 15.2%, and after the grouting repair, the increase in the maximum value of absolute principal stress and the maximum value of absolute minimum principal stress was 11.2% and 4.5% compared with the normal condition, and the increase was reduced by 8.3% and 9.5% compared with the increase when the top was void. The maximum values of absolute values of maximum principal stress under the EL-Centro wave are 0.187 MPa, 0.233 MPa, and 0.208 MPa, respectively. The maximum values of the absolute minimum principal stress at the top of the secondary lining in normal conditions, when the top is void, and after grouting repair are 6.57 MPa, 7.55 MPa, and 6.95 MPa, respectively, compared with the normal
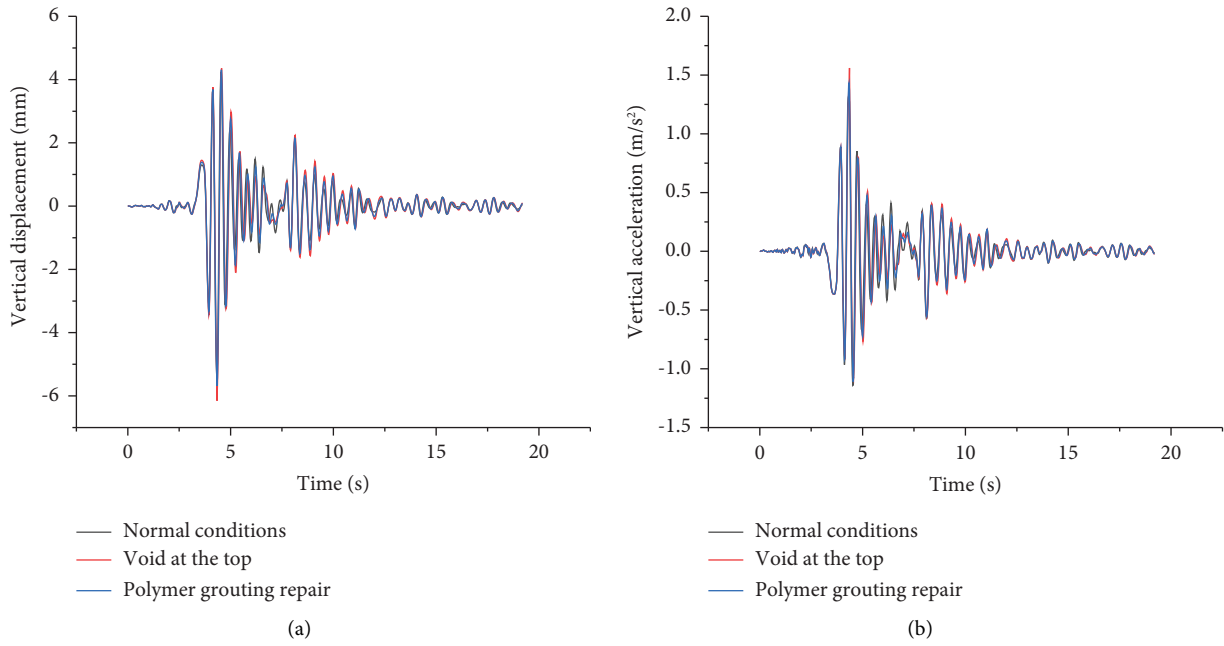
FIGURE 16: Vertical displacement and acceleration time curves of the top of the secondary lining under different working conditions of the tunnel under the action of the Northridge wave (Class I site): (a) the time course curve of vertical displacement at the top of the secondary lining; (b) the time course curve of vertical acceleration at the top of the secondary lining.
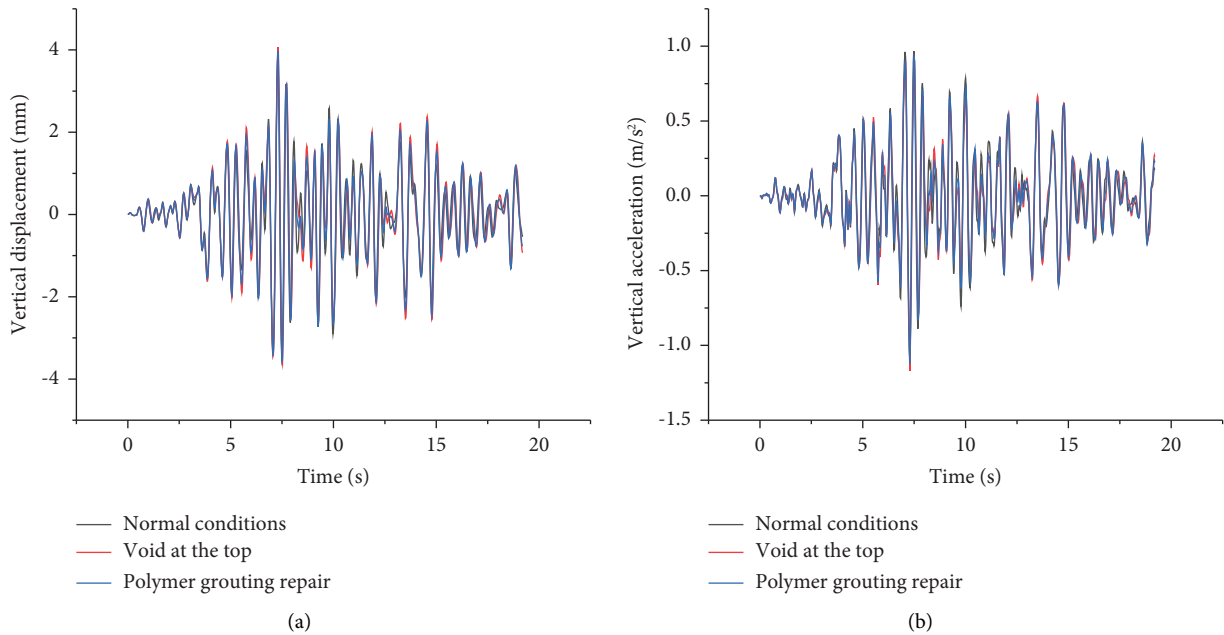


FIGURE 17: Vertical displacement and acceleration time curves of the top of the secondary lining under different working conditions of the tunnel under the action of Taft waves (Class II site): (a) the time course curve of vertical displacement at the top of the secondary lining; (b) the time course curve of vertical acceleration at the top of the secondary lining.

condition, when the top is void compared with the normal condition, the increase in the maximum absolute value of the maximum principal stress and the minimum absolute value of the principal stress at the top of the secondary lining was 24.6% and 14.9%, and after the grouting repair, the increase in the maximum absolute value of the maximum principal stress and the minimum absolute value of the principal stress was 11.2% and 5.8% compared with the normal condition, and the increase decreased by 10.7% and 7.9% compared with the top of the lining when the top was void. Compared with the top void condition, the compressive stress at the top of the secondary lining after grouting repair is obviously
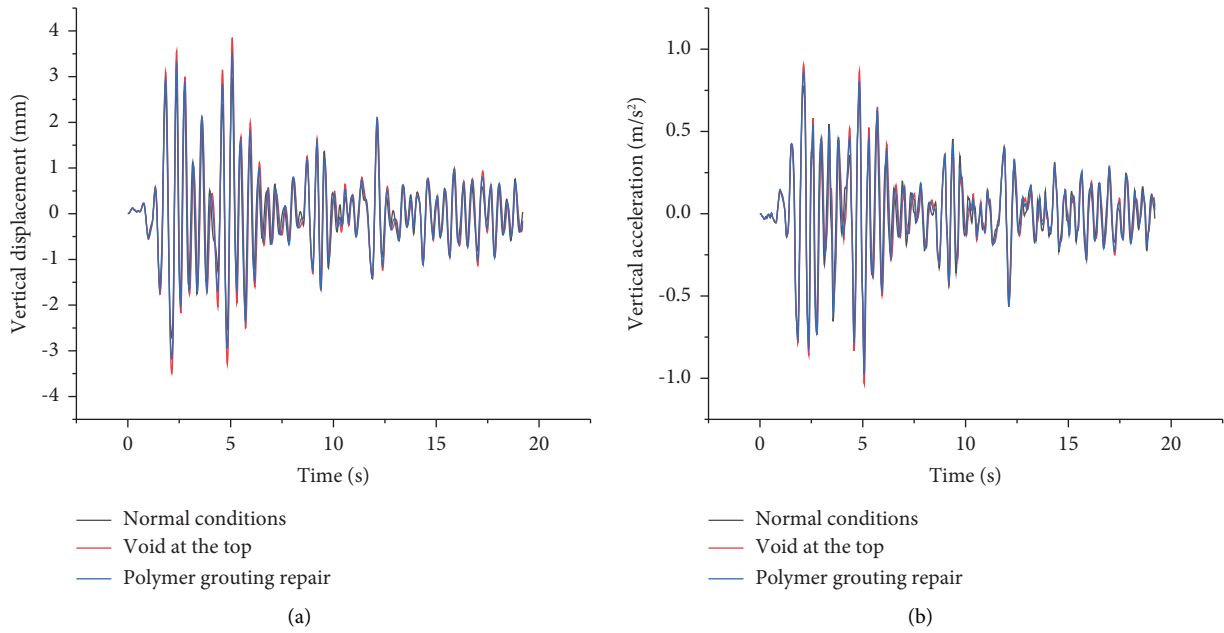
FIGURE 18: Vertical displacement and acceleration time curves of the top of the secondary lining under different working conditions of the tunnel under the action of the EL-Centro wave (Class III site): (a) the time course curve of vertical displacement at the top of the secondary lining; (b) the time course curve of vertical acceleration at the top of the secondary lining.
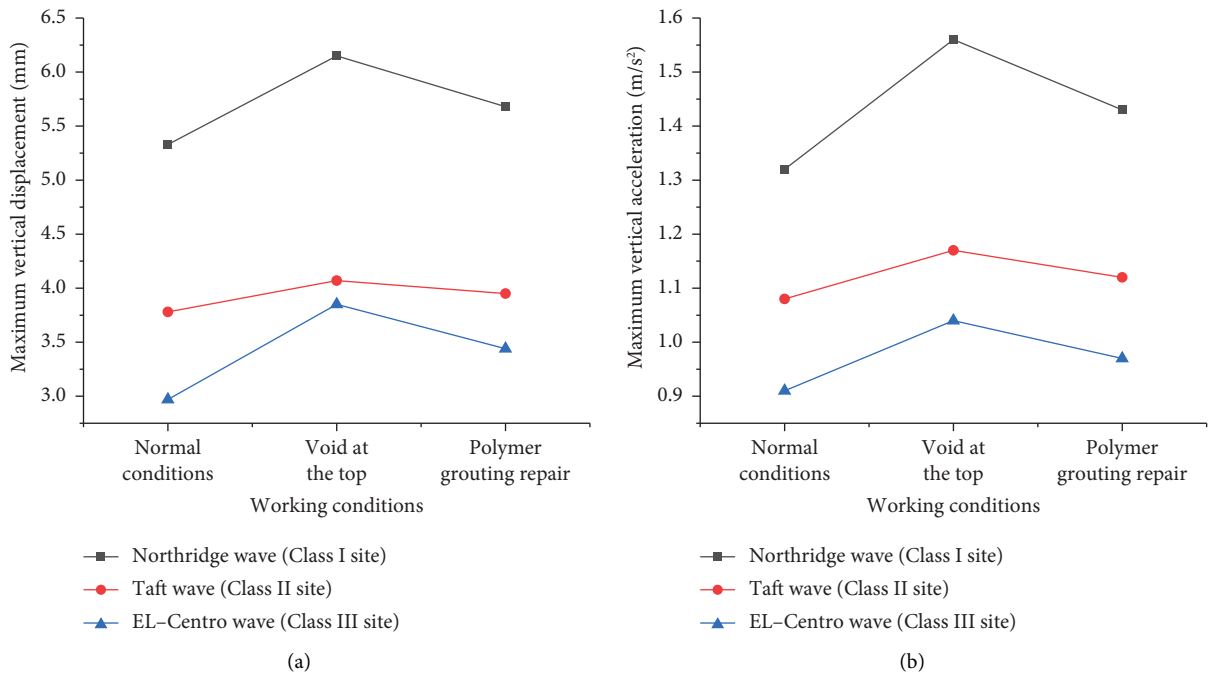


FIGURE 19: The maximum vertical displacement and maximum vertical acceleration of the top of the secondary lining of the tunnel under the action of seismic waves at different sites: (a) the maximum vertical displacement of the top of the secondary lining; (b) the maximum vertical acceleration at the top of the secondary lining.

small and close to the normal condition, which achieves the expected repair effect and makes the overall force deformation of the support structure safer and more stable.

It can be seen from Figure 23 that, under the action of seismic waves with the same peak value in different site conditions, there are obvious differences between the

maximum absolute value of the maximum principal stress and the maximum absolute value of the minimum principal stress at the top of the secondary lining. The maximum absolute value of the maximum principal stress and the maximum absolute value of the minimum principal stress under Northridge wave (type I site) excitation are the largest,
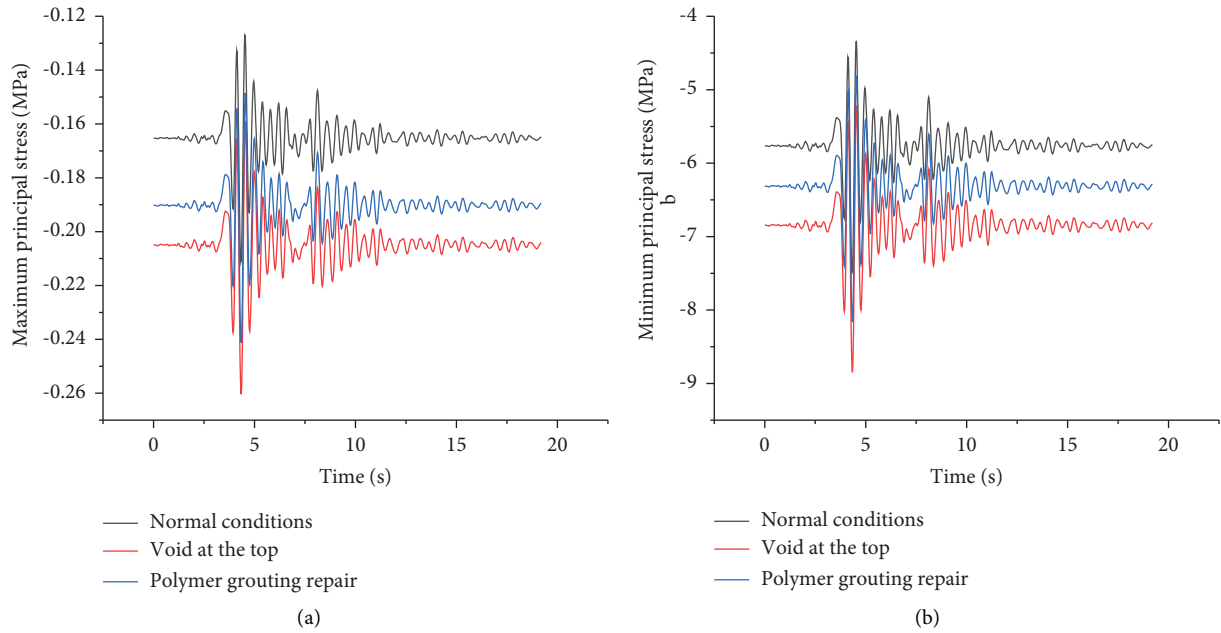
FIGURE 20: Stress variation curves at the top of the secondary lining for different working conditions of the tunnel under the action of the Northridge waves (Class I site): (a) the variation curve of the maximum principal stress at the top of the secondary lining; (b) A minimum principal stress variation curve at the top of the secondary lining.
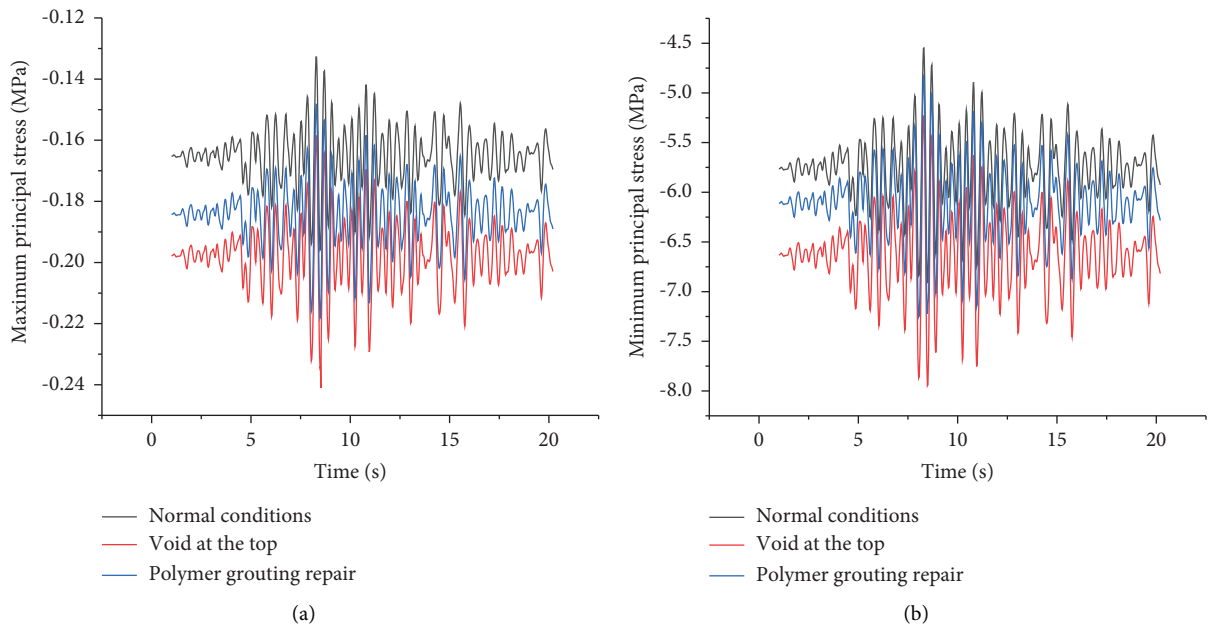


FIGURE 21: Stress variation curves of the top of the secondary lining under different working conditions of the tunnel under the action of the Taft waves (Class II site): (a) the variation curve of the maximum principal stress at the top of the secondary lining; (b) a minimum principal stress variation curve at the top of the secondary lining.

and the maximum absolute value of the vertical maximum principal stress under the excitation of EL-Centro wave (type III site), The maximum value of the absolute value of the minimum principal stress is the smallest; that is, as the site

type changes from hard, medium hard, to medium soft, the stress effect on the top of the secondary lining gradually weakens, indicating that the dynamic response of the tunnel model has obvious sensitivity to the seismic wave spectrum.
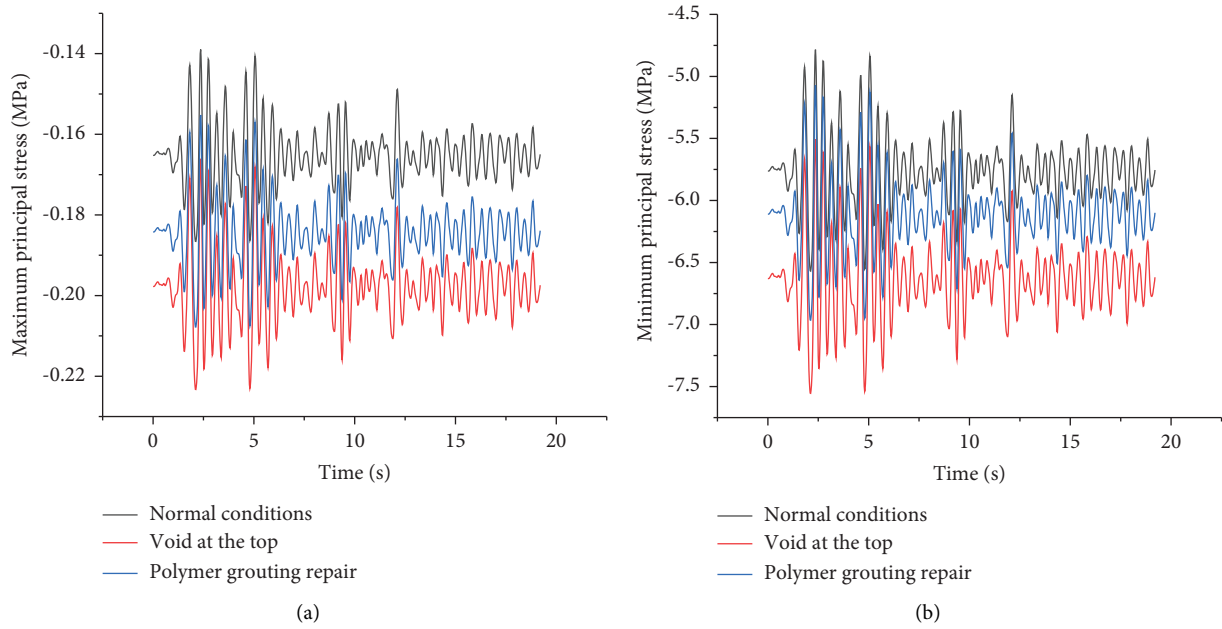
Figure 22: Stress variation curves at the top of the secondary lining for different working conditions of the tunnel under the action of the EL-Centro wave (Class III site): (a) the variation curve of the maximum principal stress at the top of the secondary lining; (b) a minimum principal stress variation curve at the top of the secondary lining.
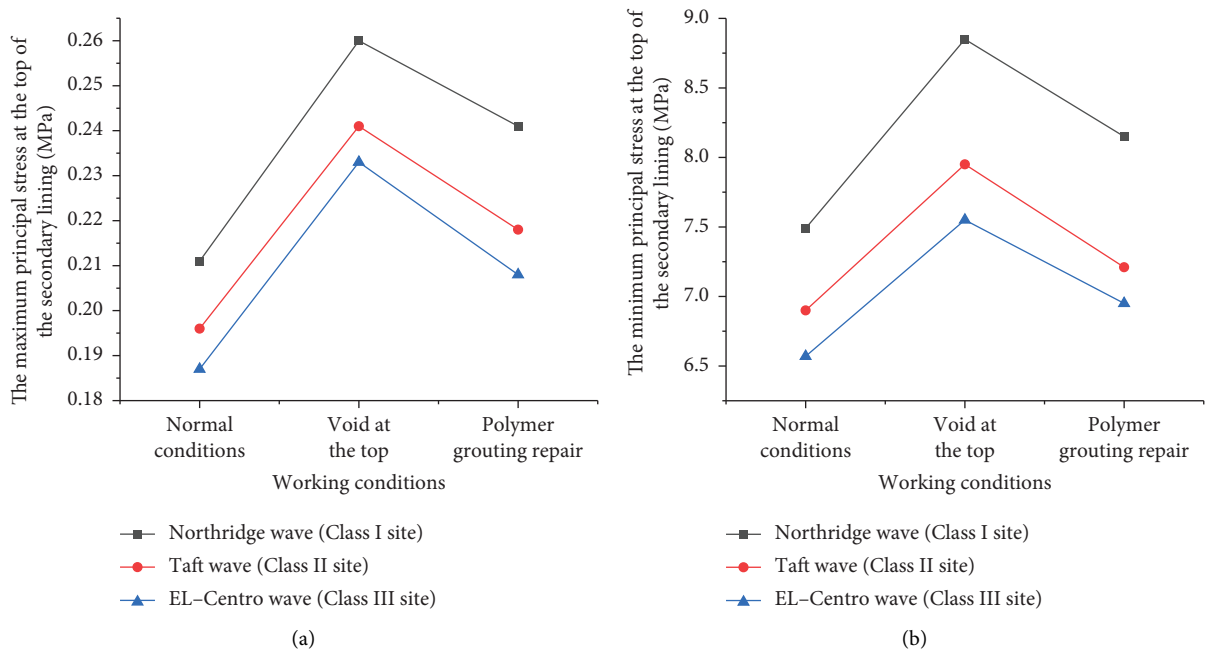


Figure 23: The maximum stress and minimum principal stress at the top of the secondary lining of the tunnel are determined by the action of seismic waves at different sites: (a) the maximum principal stress at the top of the secondary lining; (b) the minimum principal stress at the top of the secondary lining.

## 6. Conclusion

In this paper, the construction process of the Longmenshan Mountain tunnel under construction was numerically simulated using the Longmenshan Mountain tunnel as the engineering background, and the inversion of the physical parameters of tunnel envelope mechanics was carried out for the grade IV envelope section using the system identification sensitivity analysis method. Finally, the analysis of the effect of high polymer grouting to repair the tunnel debonding was carried out under the seismic mechanical response, and the following conclusions were obtained:

(1) Numerical simulation of the Longmenshan Mountain tunnel project using finite element software, found that the deformation law and stress distribution law of its tunnel envelope and support structure are in line with the site construction, but the amount of deformation such as vault settlement and peripheral convergence is different from the actual monitoring and measurement data, and this difference is caused by the discrepancy between the surrounding rock mechanical parameters selected by the numerical model and the actual difference is mainly caused by the discrepancy between the surrounding rock mechanical parameters selected by the numerical model and the actual ones.

(2) Based on the system identification sensitivity analysis method, the two-dimensional parameter inversion method is improved, the formula for three-dimensional physical and mechanical parameter inversion analysis of the surrounding rock is derived, and the three-dimensional mechanical parameter inversion analysis of the surrounding rock in the right line of the Longmenshan tunnel section from K83 + 010 to K83 + 90 is carried out. The final mechanical parameters of the surrounding rock, in line with reality, are the static elastic modulus $E_s = 1.82$ GPa, Poisson's ratio $\mu = 0.32$, and the internal friction angle $\varphi = 35°$, proving the feasibility of the system identification sensitivity analysis method. It has an important reference value for the real-time detection of the Longmenshan tunnel project under construction and provides a guarantee for accurately establishing the finite element model of the overall structure of the tunnel and surrounding rock and carrying out dynamic response analysis.

(3) The seismic mechanical response analysis verified the significant effect of polymer grouting to repair the tunnel debonding. The displacement and stress at the top of the tunnel's secondary liner debonding area were significantly reduced after the slurry repair, which was close to the normal condition. However, the stress and displacement of the top of the secondary lining under the action of seismic waves from the same peak at different site conditions are significantly different, and the effect on the displacement and stress response of the top of the secondary

lining gradually decreases as the site type changes from hard, medium hard, to medium soft, indicating that the dynamic response of this tunnel model has obvious sensitivity to the seismic wave spectrum.

## Data Availability

The data presented in this study are available in the main text of the article.

## Conflicts of Interest

The authors declare that they have no conflicts of interest regarding the publication of this paper.

## Acknowledgments

## References

[1] X. Zhang, Y. Jiang, and K. Maegawa, "Mountain tunnel under earthquake force: a review of possible causes of damages and restoration methods," *Journal of Rock Mechanics and Geotechnical Engineering*, vol. 12, no. 2, pp. 414–426, 2020.

[2] F. Ye, N. Qin, X. Liang, A. Ouyang, Z. Qin, and E. Su, "Analyses of the defects in highway tunnels in China," *Tunnelling and Underground Space Technology*, vol. 107, Article ID 103658, 2021.

[3] P. Li, C. Feng, H. Liu, Y. Zhao, Z. Li, and H. Xiong, "Development and assessment of a water pressure reduction system for lining invert of underwater tunnels," *Marine Georesources and Geotechnology*, vol. 39, no. 3, pp. 365–371, 2021.

[4] Y. Luo and J. Chen, "Research status and progress of tunnel frost damage," *Journal of Traffic and Transportation Engineering*, vol. 6, no. 3, pp. 297–309, 2019.

[5] J. Fu, J. Xie, S. Wang, J. Yang, F. Yang, and H. Pu, "Cracking performance of an operational tunnel lining due to local construction defects," *International Journal of Geomechanics*, vol. 19, no. 4, Article ID 4019019, 2019.

[6] C. L. Xin, Z. Z. Wang, and B. Gao, "Shaking table tests on seismic response and damage mode of tunnel linings in diverse tunnel-void interaction states," *Tunnelling and Underground Space Technology*, vol. 77, pp. 295–304, 2018.

[7] N. Yasuda, K. Tsukada, and T. Asakura, "Three-dimensional seismic response of a cylindrical tunnel with voids behind the lining," *Tunnelling and Underground Space Technology*, vol. 84, pp. 399–412, 2019.

[8] B. Min, C. Zhang, X. Zhang, H. Wang, P. Li, and D. Zhang, "Cracking performance of asymmetric double-arch tunnels due to the voids behind linings," *Thin-Walled Structures*, vol. 154, Article ID 106856, 2020.

[9] J. X. Zhang, N. Zhang, A. Zhou, and S. L. Shen, "Numerical evaluation of segmental tunnel lining with voids in outside backfill," *Underground Space*, vol. 7, no. 5, pp. 786–797, 2022.

[10] L. Jin-long, O. Hamza, K. Sian Davies-Vollum, and L. Jie-qun, "Repairing a shield tunnel damaged by secondary grouting," *Tunnelling and Underground Space Technology*, vol. 80, pp. 313–321, 2018.

[11] P. Zhou, M. Lin, F. Zhou, L. Gong, and W. Ao, "Bearing characteristics and failure mechanism of a novel plate-short anchor structure for tunnel crack reinforcement," *Engineering Failure Analysis*, vol. 135, Article ID 106160, 2022.

[12] W. Han, Y. Jiang, N. Li, G. Wang, H. Luan, and C. Liu, "Failure behavior and reinforcing design of degraded tunnel linings based on the three-dimensional numerical evaluation," *Engineering Failure Analysis*, vol. 129, Article ID 105677, 2021.

[13] C. Liu, D. Zhang, and S. Zhang, "Characteristics and treatment measures of lining damage: a case study on a mountain tunnel," *Engineering Failure Analysis*, vol. 128, Article ID 105595, 2021.

[14] M. Shi, F. Wang, and J. Luo, "Compressive strength of polymer grouting material at different temperatures," *Journal of Wuhan University of Technology-Materials Science Edition*, vol. 25, no. 6, pp. 962–965, 2010.

[15] F. M. Wang, M. S. Shi, H. J. Li, and Y. H. Zhong, "Experimental study on the anti-permeability properties of polymer grouting materials," *Advanced Materials Research*, vol. 284-286, pp. 1952–1955, 2011.

[16] R. Wang, F. Wang, J. Xu, Y. Zhong, and S. Li, "Full-scale experimental study of the dynamic performance of buried drainage pipes under polymer grouting trenchless rehabilitation," *Ocean Engineering*, vol. 181, pp. 121–133, 2019.

[17] H. Fang, B. Li, F. Wang, Y. Wang, and C. Cui, "The mechanical behaviour of drainage pipeline under traffic load before and after polymer grouting trenchless repairing," *Tunnelling and Underground Space Technology*, vol. 74, pp. 185–194, 2018.

[18] B. Li, F. Wang, H. Fang, K. Yang, X. Zhang, and Y. Ji, "Experimental and numerical study on polymer grouting pretreatment technology in void and corroded concrete pipes," *Tunnelling and Underground Space Technology*, vol. 113, Article ID 103842, 2021.

[19] H. Fang, Y. Su, X. Du, F. Wang, and B. Li, "Experimental and numerical investigation on repairing effect of polymer grouting for settlement of high-speed railway unballasted track," *Applied Sciences*, vol. 9, no. 21, p. 4496, 2019.

[20] X. Bian, X. Duan, W. Li, and J. Jiang, "Track settlement restoration of ballastless high-speed railway using polyurethane grouting: full-scale model testing," *Transportation Geotechnics*, vol. 26, Article ID 100381, 2021.

[21] S. Li, Y. Niu, B. Wang, Y. Gao, and Y. Zhu, "Research on mechanical response of polymer grouting repair for longitudinal cracks in reconstructed and expanded expressway pavement," *Mathematical Problems in Engineering*, vol. 2022, Article ID 5760674, 8 pages, 2022.

[22] C. Cui, Q. Lu, C. Guo, and F. Wang, "Analysis of the coupling effect of thermal and traffic loads on cement concrete pavement with voids repaired with polymer grout," *Advances in Materials Science and Engineering*, vol. 2022, Article ID 2517250, 17 pages, 2022.

[23] V. Vemuri, J. A. Dracup, R. C. Erdmann, and N. Vemuri, "Sensitivity analysis method of system identification and its potential in hydrologic research," *Water Resources Research*, vol. 5, no. 2, pp. 341–349, 1969.

[24] A. A. Javadi, R. Farmani, V. V. Toropov, and C. Snee, "Identification of parameters for air permeability of shotcrete tunnel lining using a genetic algorithm," *Computers and Geotechnics*, vol. 25, no. 1, pp. 1–24, 1999.

[25] Y. M. A. Hashash, S. Levasseur, A. Osouli, R. Finno, and Y. Malecot, "Comparison of two inverse analysis techniques for learning deep excavation response," *Computers and Geotechnics*, vol. 37, no. 3, pp. 323–333, 2010.

[26] L. T. Nguyen and T. Nestorović, "Unscented hybrid simulated annealing for fast inversion of tunnel seismic waves," *Computer Methods in Applied Mechanics and Engineering*, vol. 301, pp. 281–299, 2016.

[27] X. Luo, H. Wang, Y. Deng, and H. Li, "Automatic inverse analysis of asphalt pavement field aging based on system identification," *IEEE Transactions on Intelligent Transportation Systems*, vol. 23, no. 11, Article ID 22106, 2022.

[28] H. B. Zhou and R. D. Li, "Back analysis of the elastic modulus and horizontal crustal stress of tunnel surrounding rock with system identification method," *Applied Mechanics and Materials*, vol. 127, pp. 412–414, 2011.

[29] F. Wang and R. L. Lytton, "System identification method for backcalculating pavement layer properties," 1993, http://onlinepubs.trb.org/Onlinepubs/trr/1993/1384/1384-001.pdf.

[30] M. Hu, Q. Zhou, Z. Ji, and L. Liang, "Study on dynamic and static modulus of rock mass in nuclear island area of some nuclear power plants in China," *Industrial Construction*, vol. 45, no. 9, pp. 37–39, 2015.